Designing a microCT instrument for planetary exploration

R.W. Obbard[1], N.T.Vo[2], P. Sarrazin[1,3]

[1]SETI Institute, 189 Bernardo Ave, Mountain View, CA, USA, robbard@seti.org
[2]Diamond Light Source, Didcot, Oxfordshire OX11 0DE, UK
[3]eXaminArt LLC, Los Altos, CA, USA

Summary

Planetary ice is a multiphase material consisting of solid ice, particulates, gas inclusions, and in some cases liquid and precipitates. The size, shape and arrangement of particulates and the size and connectivity of voids can reveal something about depositional history and past climate. The North Polar Layered Deposits (NPLD) of Mars are a multi-kilometer thick sequence of dusty-ice layers thought to record previous climatic conditions much like Earth's ice sheets record terrestrial climate fluctuations in their stratigraphy. Deciphering this polar record has been, and remains today, a major goal of Mars research (Byrne, 2009). Layers in the NPLD can be detected with remote sensing (Fishbaugh et al., 2010; Herkenhoff et al., 2007; Lalich et al., 2017), but their detailed analysis on a subcentimeter scale requires *in situ* instrumentation.

MicroCT is a nondestructive three-dimensional analysis technique that has been used by the geophysical science community for many years. Even the smallest commercial units, however, are not portable, much less suited for space travel. To examine the contents of the Mars polar caps *in situ*, we are building a miniaturised system suitable for remote use (Sarrazin et al., 2020).

Alignment by an expert technician is typically required for complex laboratory equipment after delivery to the site where it will be used. This will not be possible for the miniaturised micro computed tomography (microCT) instrument we are developing for use on a rover or lander as part of a future robotic science mission to Mars's North Polar Layered Deposits.

Introduction

Volumetric microscopy is key to nondestructive analysis of interior features in many fields of science. One of these is the study of planetary ices, including ice sheets, glaciers, sea ice, and, soon, icy deposits on other celestial bodies. Inclusions in ice are often visible to the naked eye, and yet, historically, the ice has been removed to analyse them (Iverson, et al., 2017). Doing so carefully can preserve some positional information to a millimeter scale, but not the precise position and orientation of particles.

It is tricky, however, to analyse inclusions in frozen samples in the laboratory because of their tendency to melt, frost, sublimate, and expand or contract in response to fluctuations in temperature. The community has developed techniques and tools that have made cryogenic scanning electron microscopy (SEM) and electron backscatter diffraction fairly routine (Prior et al., 2015). Synchrotron X-ray topography and transmission electron microscopy have been used to examine dislocation/grain boundary interactions in ice (Baker and Liu, 1993). Synchrotron X-ray fluorescence (XRF) spectroscopy has been used to map brine and air inclusions in sea ice (Obbard et al., 2016). Confocal Raman spectroscopy has been used for identification of inorganic and organic inclusions in the subglacial Antarctic Lake Vostok ice (Böttger et al., 2017). One of the most successful *in situ* microstructural characterisation techniques developed for Earth's ices, however, is X-ray micro computed tomography.

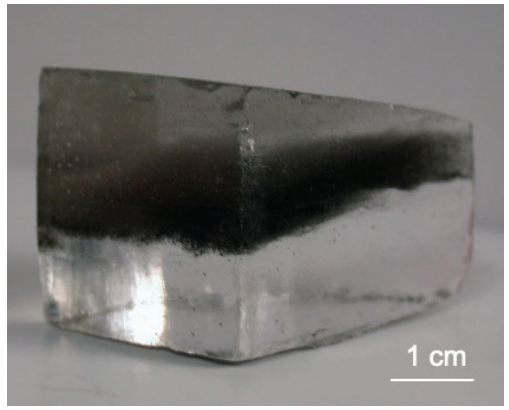

Figure 1. Photograph of ash in a sample of West Antarctic Ice Sheet (WAIS) Divide ice core WD06A, sample depth 3149.110-3149.150 m.

Meteoric ice, that which forms from precipitation, initially contains gas inclusions and can contain distinct layers of ash from volcanoes and forest fires. Volcanic tephra layers are found in many ice cores from Antarctica and a layer found across multiple cores creates a horizon that can be used to adjust ice time scales. Tephra layers can be magmatic or phreatomagmatic in nature, the latter result from explosions under ice (or water) and thus rapid cooling and thermal contraction that leads to blocky particles with few vesicules. To identify a layer, a core sample, such as that shown in Figure 1, is melted and filtered or centrifuged so that the tephra shards can be examined with SEM imagery and quantitative geochemistry (Iverson et al., 2017a). The melting and collection process, however, typically erases any segregation of particles by size or shape that was present in the ice.

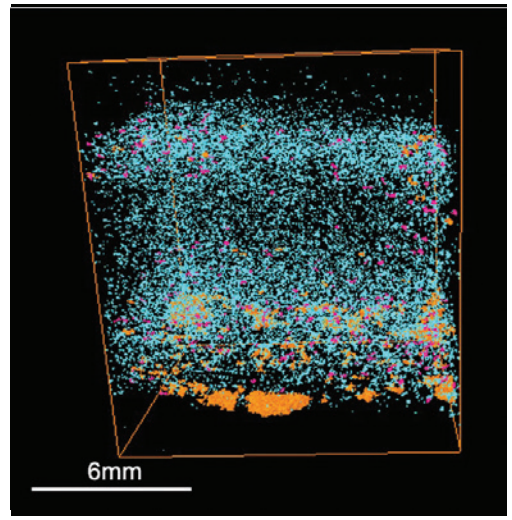

Figure 2. Reconstruction of particles in ash layer in a sample of WAIS Divide ice core WD06A, sample depth 2569.525 - 2569.555 m, with particles size color coded. Small particles (0.844 - 1.688 x 10^{-3} mm^3) are blue, medium particles (1.688 - 3.375 x 10^{-3} mm^3) are pink, large particles (> 3.375 x 10^{-3} mm^3) are orange.

We used *in situ* microCT as a complementary technique to examine the particle size and shape distribution in seven different ash layers in the West Antarctic Ice Sheet (WAIS) Divide ice core (WDC06A). Based on their chemical signatures, some tephra layers were identified as being from Mt. Berlin, Antarctica, whose eruptions are recorded in

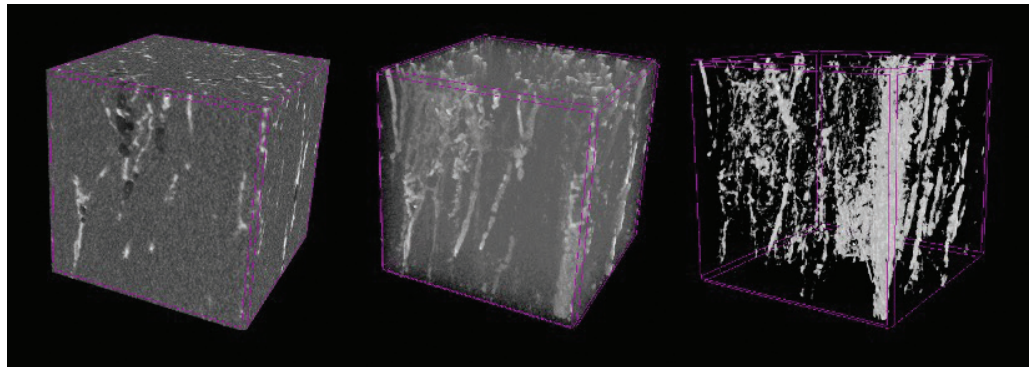

Figure 3. Brine network in sea ice from 130 cm depth, Ross Sea, Antarctica. Images from left to right show segmentation of brine from water ice. Each volume of interest is 7.5 mm/side.

other Antarctic cores. The chemical compositions of two layers, however, were quite different from these, and the tephra in size and shape was characteristic of phreatomagmatic eruptions. Our analysis identified two hitherto unknown subglacial eruptions with mixed magmatic and phreatomagmatic phases interrupting what were predominantly phreatomagmatic events (Iverson et al., 2017b).

Sea ice plays an important part in the polar ecosystem and Earth's climate. It is complex and heterogeneous, a three-phase system consisting of ice, salt precipitates, liquid brine, and gas bubbles, and its physical properties (acoustic, electrical and optical) are time and temperature dependent. These properties are heavily dependent on the internal structure of sea ice, especially its porosity, which has long been of interest to the scientific community. While optical methods are still used to examine porosity and brine networks (e.g. Light et al., 2003), microCT has enabled the non-destructive examination of these features in three dimensions on a much finer scale as shown in Figure 3 (Obbard, Troderman, & Baker, 2009) and the analysis and modeling of the brine network structure in sea ice (Lieb-Lappen, Golden, & Obbard, 2017; Lieb-Lappen et al., 2017).

Like Earth, Mars is a terrestrial planet with a climate driven by many complex factors including its orbits, geology, and volatiles. It holds a record of its recent climate in North and South Polar Layered Deposits (NPLD & SPLD), analogous to Earth's polar caps, and offers a unique opportunity to study the effects of large orbital changes on a planet lacking significant current geological activity or anthropogenic interference. The NPLD & SPLD, each greater than 2 km thick, have been examined with remote imagery and contain thousands of layers, composed of water ice, dust, salts, geochemical weathering products, trapped gasses, and other materials including cosmogenic nuclides, which are expected to contain information on the planet's climatic history. Ice accumulation rates on Mars's polar caps vary through time but are typically 0.5 mm/yr (Becerra, Sori, & Byrne, 2017). The resolution of layer observations from remote sensing, however, is coarse and cannot be used to examine layer properties and infer climatic information.

Therefore, we need to examine samples of polar ice with higher resolution methods such as microCT, which can provide information about densification, layer thickness and morphology, as well as particle size and type. The average dust content of the NPLD is only 2 to 5% (Grima et al., 2009), but most of that may be concentrated in sublimation lags that are almost pure dust (Philipps et al., 2008). While direct observation of porosity on the NPLD are lacking, models of Mars's polar accumulation suggest that densification may be rapid with a thin or absent firn layer (Arthern, Winebrenner, & Waddington, 2000). Initial porosity at the surface before layer burial might tell us about the deposition mode of the ice - i.e. snowfall vs. direct condensation.

Computed tomography is done on many scales, from the macro to the nano. A sample sits between an X-ray source and detector and either the sample or the source and detector rotate step-by-step in order to capture X-ray attenuation images at a variety of angles between 0° and 180° or 360°. These are reconstructed into a 3D model of a volume of interest in the sample. One of the advantages of microCT is that no special sample preparation is required and, in this sense, it is a method well suited for remote *in situ* use. The X-ray source in smaller systems, including desktop systems sold commercially, is typically cone beam, and the sample is rotated between the source and the detector. Even smaller systems, however, can be the size of a piece of furniture and weigh hundreds of pounds, and this greatly limits their portability.

We are developing a miniaturised instrument for in situ microCT analysis in a rover or lander as part of a future robotic science mission to Mars. The instrument would face an environment with gravity one third that on Earth (3.711 m/s^2), an atmospheric pressure several orders of magnitude less than Earth's (0.4 – 0.87 kPa), an average temperature of -46°C and polar temperatures in summer as low as -125°C (Smith et al. 2020).

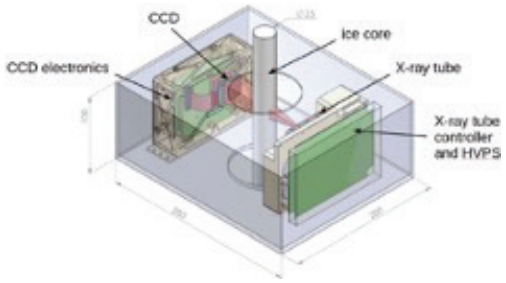

Figure 4. Architecture of the analytical head of the prototype MIST microCT subsystem.

Beyond the obvious environmental challenges are those of any instrument designed for planetary use, namely limitations on size, power, computing, and communications bandwidth and the need to be robust enough to withstand space travel and then to be operated without human intervention. This is the challenge for which we are designing the Micro In Situ Tomography system.

Methodology

MIST is a coupled sample coring and microCT analysis system. A robotic coring drill developed by Honeybee Robotics (Altadena, CA) will produce a 2.5 cm diameter sample core and capture it within an X-ray transparent tube. As this tube is withdrawn from the surface, it will be lifted through a miniaturised microCT system which will rotate around it in controlled vertical steps. At each vertical step, the core will be rotated 360° in steps of ~ 1°, and an X-ray attenuation image will be taken at each position. When the scan is complete, the core will be released. Raw X-ray attenuation images will be transmitted back to Earth for processing.

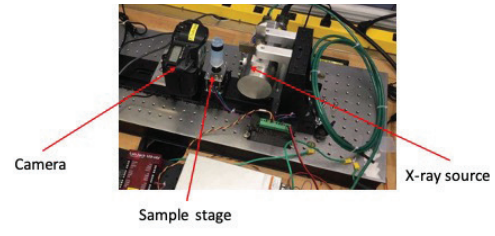

Figure 5. MIST microCT breadboard prototype.

The MIST microCT analysis subsystem will include a focused X-ray source, detection capability, and electronics to control scanning. The design of the current laboratory prototype instrument is shown in Figure 4.

Source

Water ice has a low linear X-ray absorption coefficient, enabling microCT analysis with relatively low X-ray energies. We have demonstrated that a 25 kV, 5 W X-ray source such as used in planetary x-ray diffraction (XRD) instruments is sufficient for ice cores of up to 25 mm diameter. For the prototype (Figure 5), we used a 60 µm spot size (RTW MCBI) X-ray tube and have achieved a resolution of 30 µm.

Detector

The imaging system requires good quantum efficiency (QE) and low noise in the spectral region of interest (here 15-25 keV). Desktop microCT systems typically use an X-ray camera with a CCD sensor, but in our prototype system we used a visible light digital single lens reflex (DSLR) camera with a 35 mm CMOS sensor. We converted the camera to an X-ray camera by removing the cover glass from the sensor and bonding a fiber optic plate (FOP) and CsI scintillator film to it.

Data processing methods and volume reconstruction

Reconstruction of the X-ray attenuation images (radiographs) produces 2D gray-scale slices stacked in the z-direction (Kak and Slaney, 1988), which are used to produce a 3D reconstruction of the sample. For preprocessing and cone-beam reconstruction we created a Python software package that can run on both GPU and CPU. This package is different from open-source software such as the Python Astra toolbox (van Aarle et al., 2016) in that it works on a complex misaligned system.

High quality reconstructed microCT images require stable and well-known system geometry,

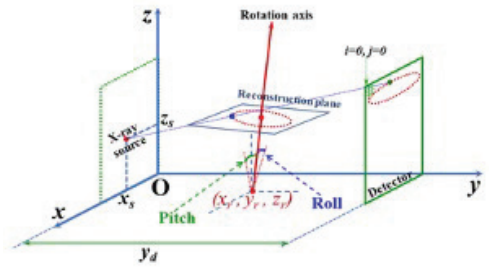

Figure 6. Misaligned cone beam geometry.

which in turn requires a stable system and regular alignment checks. A prototype microCT system – like a fully developed system after space flight – might be expected to have some slight geometrical misalignment that the software needs to be able to detect and correct for. Our cone-beam reconstruction methods are optimised for complex misaligned systems. We have developed a method for retrieving the actual geometric parameters of the cone-beam tomography system by analysing the trajectory of a point-like sample (e.g. spheres embedded in the coring sleeve wall) at two heights. Reconstruction is based on a back-projection and filtering (BPF) approach (Gullberg, 1979; Suzuki & Yamaguchi, 1988) and a filtered back-projection (FBP) approach (Kak and Slaney, 1988) incorporating all geometric parameters of a cone beam system: the pitch, roll, and positions of the rotation axis; the X-ray source positions; and the source-detector distance.

Preprocessing steps include flat-field correction, zinger removal, ring artifact removal, and beam hardening correction (Vo, Atwood & Drakopoulos, 2019) as shown in Figure 7 and Figure 8.

Simulation of ice core with inclusions

For testing, we produced test samples with ice simulant and actual ice. Ice simulant samples for room temperature microCT tests were made of wax. Chemistry grade paraffin wax (SAKURA Processing/ Embedding medium #4005, melting point: 56°C) was melted and cast in 25 mm ID (internal diameter) tubes. After a first cast, the cores are partially pushed out of the tube and trimmed to remove the upper section (~2/3) where there is a deep cavity caused by the dramatic shrinkage paraffin experiences during solidification. Inclusions were then placed on the section plane, and when needed, pushed in slightly after softening the surface with a heat gun. The core was then pushed back into the casting tube and a second cast was made. A blue dye was used in some cases to better reveal the boundary between the two casts. Using this method, we prepared wax cores with several types of inclusions: 1.6 mm steel balls, 0.8 mm Al balls, basalt grains, and quartz grains.

Ice samples for micro CT testing were frozen at Honeybee Robotics using molds. A two-step process allowed the insertion of particles at the interface between two casts. Samples were prepared with the same type of inclusions that were used for the wax rods.

We tested these at X-ray tube voltages up to 50 kV and found that good signal and measurable contrast for small inclusions is achievable at voltages as low as 25 kV. The drop in signal is, however, quite severe under 20 kV. Based on actual tests and simulations, we have concluded that 25 kV is a reasonable target for an ice core imager.

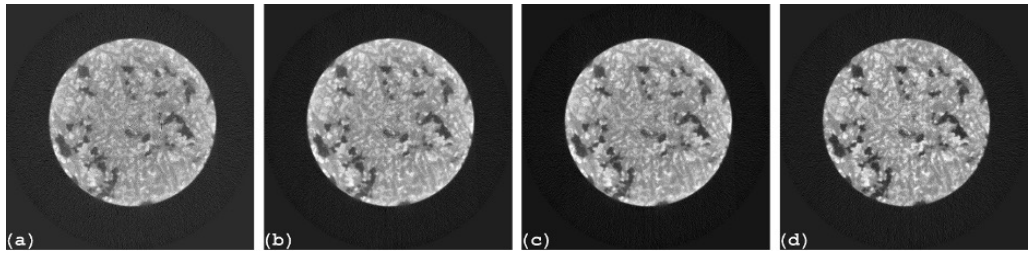

Figure 7. Reconstructed images of a rock core sample scanned by our Planetary In-situ X-ray Imager [https://examinart.com/PIXI/] at different processing stages: (a) After the flat-field correction; (b) After the zinger removal; (c) After the ring artifact removal; (d) After the beam hardening correction.

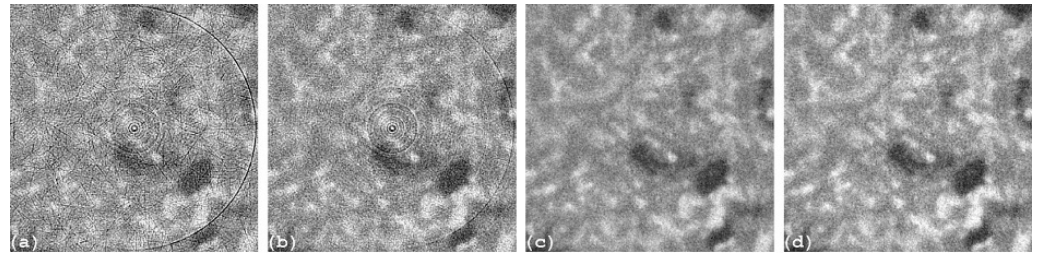

Figure 8. (a) Magnified view from the middle area of Fig. 7(a); (b) Magnified view from the middle area of Fig. 7(b); (c) Magnified view from the middle area of Fig. 7(c); (d) Magnified view from the middle area of Fig. 7(d).

Verification of the linear response of the CsI-CMOS camera

In a microCT, the signal measured is composed of a range of energies defined by the voltage and nature of the X-ray source, and the materials differentially absorbing these energies. The spectrum of the signal varies when the tube high voltage (HV) is changed. However, the spectrum is not modified when changing the beam current, it is simply scaled up and down.

We used the linear relationship between the intensity of X-ray emitted and the beam current to evaluate the linearity of the X-ray camera response; data were collected at increasing beam currents, all other parameters being preserved.

We observed poor linearity of the camera response when using in-camera JPEG compression, which does not preserve luminance. Data acquired in RAW format, with dedicated code to open these files and handle the Bayer pattern of the colour sensor, recovered a perfectly linear behavior of the X-ray sensor. This finding led to the development of a method for obtaining quantitative measurements with a digital photographic camera. Scans collected using RAW format were of higher quality than earlier scans because more accurate image correction methods could be applied (background correction, flat-fielding, etc.).

Computer modeling: Development of a spectral model

We developed a spectral simulation model of the instrument for evaluating throughput as a function of sample, X-ray tube HV, and detector type. The model is essentially composed of two modules written in Python 2.7: an emission spectrum module, and an X-ray attenuation module. The detector spectral sensitivity is computed with the X-ray attenuation module, using the chemistry and thickness of the scintillator film (CsI in our case, either 50 or 150 µm thickness). The number of photons emitted by a scintillator is proportional to the energy of the X-ray absorbed, so the light output of the scintillator is computed with the integral of the spectrum absorbed in the scintillator film. The model, whose accuracy was validated, proved quite useful. We are able to accurately predict the signal generated in the scintillator and collected by the image sensor. Key parameters such as tube voltage, filters, and sample nature and thickness can be studied at the spectral level with this tool.

Effect of filters

Aluminium filters are often used in microCT to combat beam hardening, an artifact that causes the edges of a homogenous sample to appear brighter than the centre. Of course, any filter placed in the beam will lower the signal collected.

We modeled the response of the scintillator in the same conditions, with and without a filter, for the same ice samples. We observed a dramatic difference in the direct beam spectra, but similar sample attenuation spectra. This showed that the aluminium filter primarily absorbs beam energies that are not useful to the analysis because they are systematically absorbed by the sample. In

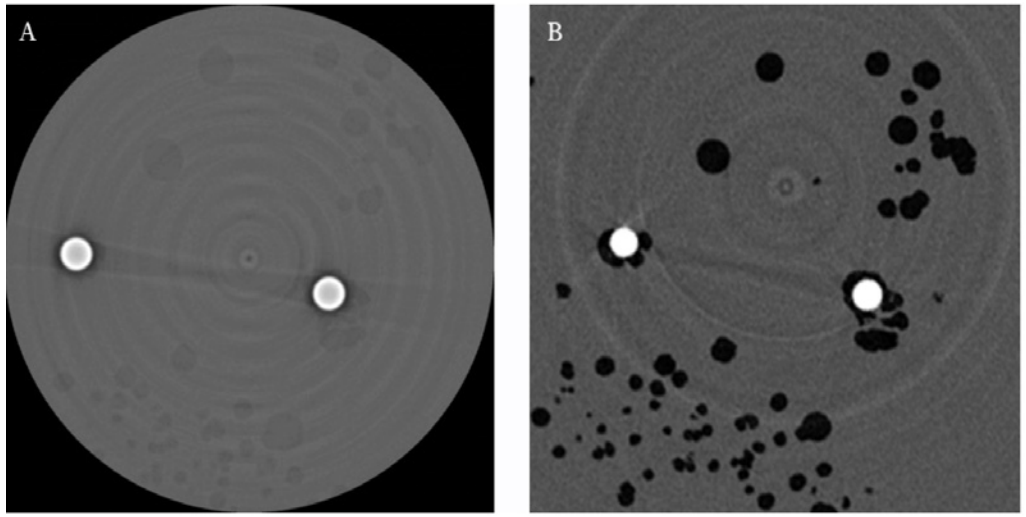

Figure 9. 3D reconstruction slice of a wax core with Al balls (0.8 mm diameter). Left: MIST data at 25 kV. Right: image from Bruker SKYSCAN 1173 at 100 kV.

the absence of the filter, the direct beam has a very different spectral characteristic than sample attenuation data. The collection of a flat-field image is necessary for processing raw projection images. If the instrument parameters are set such that a direct exposure of the sensor doesn't result in pixel saturation in the absence of an Al filter, the attenuation images will use the bottom of the camera dynamic range and lead to noisy data. With the aluminium filter, the camera dynamic range is better utilised and data with lower noise are obtained (though with longer acquisition time). We started our experimentation with the breadboard without a filter, but after observation of this effect, we adopted an aluminium filter as standard (0.5, 1 or 1.5 mm).

The prototype instrument was used for collecting data on ice core and ice core simulant samples. Most scans were collected at 400 steps/turn (0.9° step) over 360°. Camera ISO settings (i.e. detector gain) were mostly 400 and 800. Exposure times varied between 4s and 6s. ISO and shutter time were adjusted depending on the X-ray tube setting and the sample attenuation.

Reconstruction was done using a NVIDIA Tesla K20C graphics card with a GK110 graphics processing unit (GPU) and 5 GB memory.

Results

As a benchmark for our results, we compared them with those obtained using a commercial system, Bruker's SKYSCAN 1173 benchtop X-ray microCT and the associated software. The instrument has a microfocus X-ray source and distortion-free 2240 x 2240 pixel 12-bit flat panel sensor with a camera pixel size of 50 µm. Source voltage was 100 keV, and current 80 µA. A 1 mm Al filter was used. Image rotation was 0.28°. Preprocessing included removal of ring and beam hardening artifacts and application of a Gaussian smoothing kernel. SKYSCAN's GPU-based NRECON reconstruction software was used to solve the inverted Radon transform, which transforms the X-ray projections using a modified Feldkamp (FDK) cone-beam algorithm to produce a stack of gray-scale cross-section images.

Data were acquired with the SKYSCAN 1173 after the corresponding MIST data had been collected and fully processed. Consequently, the reference data did not influence the way the MIST data was collected or processed in any way. No adjustment was done to either the MIST 3D slice images or the SKYSCAN 3D slice images shown in the following figures, other than flips and rotations to place them in the same orientations.

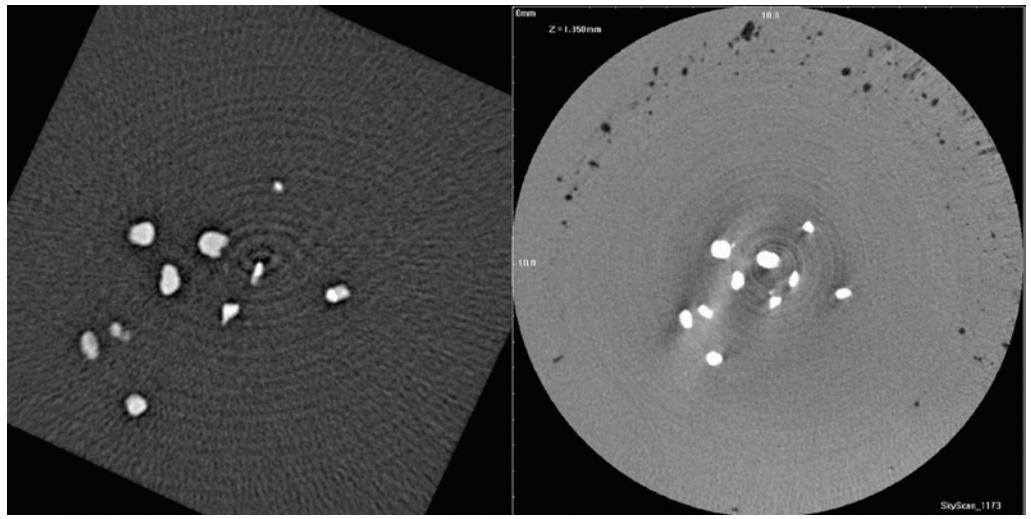

Figure 10. 3D reconstruction slice of a 25 mm diameter ice core with large sand grains. Left: MIST data. Right: Bruker SKYSCAN 1173 image. Ring artifacts in the MIST data come from inappropriate image corrections due to the JPEG projection image format used for the early data set.

Wax core for calibration — Figure 9 compares a slice of the reconstructed wax core sample scanned and reconstructed with our 25 kV system (left) to a slice from nominally the same height in the sample acquired with the commercial instrument (SKYSCAN 1173, 100 kV) (right). Source energy, placement of the sample relative to the axis of rotation, and volume scanned were different, hence the differences in the background (and ring artifacts). Note, however, that the same features and spacing are visible in both images, including not only the two Al balls (white) but the voids in the wax (darker grey left, black right).

Ice core — Figure 10 shows equivalent slices of two 3D reconstructions of an ice core with coarse sand grains. MIST data, collected after moving the breadboard to a -25°C walk-in freezer, are compared to lab data obtained from a SKYSCAN instrument with cold temperature stage. Both data show similar features but ring artifacts are observed with MIST. This was later found to be associated with the JPEG format used to save the camera images. The data nonetheless demonstrates that 3D reconstruction of ice cores with inclusions can be obtained with good resolution

Discussion and Conclusion

The MIST microCT breadboard system we have developed can correct for misaligned geometry and, using RAW images of a rock core, we have achieved 30 µm resolution. Although this could resolve the annual layers in the NPLD, we are replacing both the source and detector to improve resolution further. We are also working with Honeybee Robotics on the coring subsystem and integration of the overall MIST system. Future work will incorporate a high-fidelity camera, flight ready electronics and hardware and improvements to data processing. We will need to address data transmission and the division of storage and processing tasks between local and remote, and we anticipate that machine learning for data reduction will be key.

MicroCT is the most comprehensive single technique to analyse the layering of the NPLD because it can provide high resolution information on densification, layer thickness and morphology, as well as particle size. It is even more powerful in a complementary setting, paired with other characterisation techniques such as X-ray diffraction (XRD), XRF, or SEM electron dispersive spectroscopy (EDS) to identify shape and volume, elemental content, and phase.

MIST, a lander or rover mounted microCT system, could provide much of the microstructural data we would seek from a Mars ice-sediment core, while avoiding the significant hurdles posed by bringing samples back to Earth.

Acknowledgements

MIST is funded by NASA grant NASA PICASSO 17-PICASO17_2-0094. This work had its inception at the W. M. Keck Institute for Space Studies and its origin in experience acquired and a need recognised under NSF Awards ANT-1142035, PLR-1304134, and PLR-1603683.

References

Arthern, R.J., Winebrenner, D.P., and Waddington, E.D. (2000) Densification of water ice deposits on the residual north polar cap of Mars. Icarus, 144, 2, 367-381.

Baker, I., and Liu, F. (1993). On In-Situ Study of Dislocation/Grain Boundary Interactions Using X-ray Topography and TEM. MRS Proceedings 319, 203. doi:10.1557/PROC-319-203

Becerra, P., Sori, M.M., and Byrne, S. (2017) Signals of astronomical climate forcing in the exposure topography of the North Polar Layered Deposits of Mars. Geophys. Res. Lett. 44(1), 62-70.

Böttger, U., Bulat, S.A., Hanke, F., Pavlov, S.G., Greiner-Bär, M., and Hübers, H.-W (2017). Identification of inorganic and organic inclusions in the subglacial Antarctic Lake Vostok ice with Raman spectroscopy. Journal of Raman Spectroscopy 48(11), 1503–1508. https://doi.org/10.1002/jrs.5142

Fishbaugh, K.E., Byrne, S., Herkenhoff, K. E., Kirk, R.L., Fortezzo, C., Russell, P. S., and McEwen, A. (2010). Evaluating the meaning of "layer" in the martian north polar layered deposits and the impact on the climate connection. Icarus 205, 1:269-282.

Grima C., Kofman,W., Mouginot, J., Phillips, R.J., Hérique, A., Biccari, D., Seu, R., and Cutigni, M. (2009). North Polar Deposits of Mars: Extreme purity of the water ice. Geophys. Res. Lett. 36, L03203, doi:10.1029/2008GL036326

Gullberg, G.T. (1979) The reconstruction of fan-beam data by filtering the back-projection. Computer Graphics and Image Processing 10, 30-47. doi: 10.1016/0146-664X(79)90033-9.

Herkenhoff, K.E., Byrne, S., Russell, P.S., Fishbaugh, K.E., and McEwen, A.S. (2007). Meter-scale morphology of the north polar region of Mars. Science 317, 5845: 1711-1715.

Iverson, N.A., Kalteyer, D., Dunbar, N.W., Kurbatov, A., and Yates, M. (2017a). Advancements and best practices for analysis and correlation of tephra and cryptotephra in ice. Quaternary Geochronology 40, 45-55. https://doi.org/10.1016/j.quageo.2016.09.008

Iverson, N. Lieb-Lappen, R., Dunbar, N.W., Obbard, R., Kim, E., and Golden E. (2017b). The first physical evidence of subglacial volcanism under the West Antarctic Ice Sheet. Nature Scientific Reports 7: 11457 (2017) DOI: 10.1038/s41598-017-11515-3

Iverson, N., Obbard, R., Lieb-Lappen, R., Kim, E., Golden, E., and Dunbar, N. (2014). Phreatomagmatic eruptions under the West Antarctic Ice Sheet: Potential hazard for ice sheet stability" V11B-4717 - American Geophysical Union (AGU) Fall Meeting, San Francisco, CA, December 15, 2014.

Kak, A. C. and Slaney, M. (1988) Principles of Computerized Tomographic Imaging, IEEE Press.

Lalich, D. E., and Holt J.W. (2017). New Martian climate constraints from radar reflectivity within the north polar layered deposits. Geophys Res. Lett., 44, 2: 657-664.

Lieb-Lappen, R.M., Golden, E.J., and Obbard R.W. (2017). Metrics for interpreting the microstructure of sea ice using micro-computed tomography. *Cold Regions Research and Technology*, June 2017, 24-37.

Lieb-Lappen, R.M., Kumar, D.D., Pauls, S.D., Obbard, R.W. (2017). A Network Model for Characterizing Brine Channels in Sea Ice. *The Cryosphere*. December 2017. DOI:10.5194/tc-2017-169

Light, B., Maykut, G.A., and Grenfell T.C. (2003). Effects of temperature on the microstructure of first-year Arctic sea ice, J. Geophys. Res. 108(C2), 3051, doi:10.1029/2001JC000887.

Obbard, R.W., Lieb-Lappen, R., Nordick, K.V., Golden, E.J., Leonard, J.R., Lanzirotti, A., and Newville, M.G. (2016). Synchrotron X-ray Fluorescence Spectroscopy of Salts in Natural Sea Ice. *Earth and Space Science*. 11/30/16 DOI:10.1002/2016EA000172

Obbard, R.W., Troderman, G., and Baker, I. (2009). Imaging brine and air inclusions in sea ice using micro X-ray computed tomography. *Journal of Glaciology* 55 (194), 1113-1115. http://www.igsoc.org/journal/55/194/

Phillips, R. J., Zuber, M. T., Smrekar, S. E., Mellon, M. T., Head, J. W., Tanaka, K. L., Putzig, N. E., Milkovich, S. M., Campbell, B. A., Plaut, J. J., Safaeinili, A., Seu, R., Biccari, D., Carter, L. M., Picardi, G., Orosei, R., Mohit, P. S., Heggy, E., Zurek, R. W., Egan, A. F., Giacomoni, E., Russo, F., Cutigni, M., Pettinelli, E., Holt, J. W., Leuschen, C. J., Marinangeli, L. (2008) Mars North Polar Deposits: Stratigraphy, Age, and Geodynamical Response. Science 320, 1182–1185. doi:10.1126/science.1157546

Prior, L., Lilly, K., Seidemann, M., Vaughan, M., Becroft, L., Easingwood, R., Diebold, S., Obbard, R., Daghlian, C., Baker, I., Caswell, T., Golding, N., Goldsby, D., Durham, W.B., Piazolo, S., and Wilson, C. (2015). Making EBSD on water ice routine. Journal of Microscopy 259(3), 237–256. https://doi.org/10.1111/jmi.12258

Sarrazin, P., Obbard, R., Vo, N., Zacny, K., Hinman, N., Lafuente, B., Chen, J., Blake, D., Bristow, T., Rampe, E., Byrne, S., and Eckley, S. (2020). In-situ microCT for planetary exploration: A White Paper Submitted to the Planetary Science and Astrobiology Decadal Survey 2023-2032. *In review.*

Smith, I.B., Hayne, P.O., Byrne, S., Becerra, P., Kahre, M., Calvin, W., Hvidberg, C., Milkovich, S., Buhler, P., Landis, M., Horgan, B., Kleinböhl, A., Perry, M.R., Obbard, R., Stern, J., Piqueux, S., Thomas, N., Zacny, K., Carter, L., Edgar, L., Emmett, J., Navarro, T., Hanley, J., Koutnik, M., Putzig, N., Henderson, B.L., Holt, J.W., Ehlmann, B., Parra, S., Lalich, D., Hansen, C., Hecht, M., Banfield, D., Herkenhoff, K., Paige, D.A., Skidmore, M., Staehle, R.L., Siegler, M., The Holy Grail: A road map for unlocking the climate record stored within Mars' polar layered deposits, Planetary and Space Science (2020), https://doi.org/10.1016/j.pss.2020.104841.

Suzuki, S. and Yamaguchi, S. (1988) Comparison between an image reconstruction method of filtering backprojection and the filtered backprojection method. Applied Optics 27, 2867-2870.

van Aarle, W., Palenstijn, W. J., Cant, J., Janssens, E., Bleichrodt, F., Dabravolski, A., De Beenhouwer, J., Batenburg, K.J., and Sijbers, J. (2016). Fast and flexible x-ray tomography using the ASTRA toolbox. Optics Express 24(22), 25129-25147. doi: 10.1364/OE.24.025129.

Vo, N. T., Atwood, R., Drakopoulos, M. (2019). Preprocessing techniques for removing artifacts in synchrotron-based tomographic images. Proceedings Volume 11113, Developments in X-Ray Tomography XII; 111131I (2019), Event: SPIE Optical Engineering + Applications, 2019, San Diego, California, United States https://doi.org/10.1117/12.2530324

Dr. Rachel W. Obbard

Rachel has a BSc in Engineering Physics, an MSc in Materials Science and Engineering, and a PhD in Engineering. She was a postdoctoral fellow at the British Antarctic Survey and now works for the SETI Institute, a non-profit research organisation. Rachel's work on the characterisation of planetary ices, which has included SEM/EDS/EBSD and synchrotron XRF as well as microCT, has taken her from the Antarctic to the Arctic and often involves the development of new tools and techniques.